

Electron heat transport from stochastic fields in gyrokinetic simulations^{a)}E. Wang,^{1,b)} W. M. Nevins,¹ J. Candy,² D. Hatch,³ P. Terry,³ and W. Guttenfelder⁴¹Lawrence Livermore National Laboratory, 7000 East Ave. L-637, Livermore, California 94550, USA²General Atomics, P.O. Box 85608, San Diego, California 92186-5608, USA³Max-Planck-Institut für Plasmaphysik, EURATOM Association, 85748, Garching, Germany⁴Princeton Plasma Physics Laboratory, P.O. Box 451, Princeton, New Jersey 08543, USA

(Received 29 November 2010; accepted 1 March 2011; published online 2 May 2011)

GYRO is used to examine the perturbed magnetic field structure generated by electromagnetic gyrokinetic simulations of the CYCLONE base case as β_e is varied from 0.1% to 0.7%, as investigated by J. Candy [Phys. Plasmas **12**, 072307 (2005)]. Poincaré surface of section plots obtained from integrating the self-consistent magnetic field demonstrates widespread stochasticity for all nonzero values of β_e . Despite widespread stochasticity of the perturbed magnetic fields, no significant increase in electron transport is observed. The magnetic diffusion, d_m [A. B. Rechester and M. N. Rosenbluth, Phys. Rev. Lett **40**, 38 (1978)], is used to quantify the degree of stochasticity and related to the electron heat transport for hundreds of time slices in each simulation. © 2011 American Institute of Physics. [doi:10.1063/1.3574660]

I. INTRODUCTION

One of the fundamental components of a steady state tokamak or stellarator fusion reactor is the integrity of nested magnetic surfaces. Loss of these magnetic surfaces can have very serious implications, ranging from sawtooth crashes to disruptions. A mechanism for destroying surfaces is electromagnetic instabilities. Gyrokinetic simulation codes are now capable of modeling plasma microturbulence including kinetic ions, electrons, and electromagnetic effects,^{1–4} allowing for study of magnetic surface integrity in the presence of the perturbed magnetic field. Gyrokinetic simulations including kinetic ions and electromagnetic effects^{2,5,6} were done about the CYCLONE (Ref. 7) base-case operating point. The strength of electromagnetic effects is quantified by the electron $\beta_e = 8\pi n_e T_e / B^2$, where n_e and T_e are the equilibrium electron density and temperature and B is the magnitude of the magnetic field. For plasmas with equal ion and electron temperatures, $2\beta_e = \beta = 8\pi p / B^2$, where p is the total plasma pressure. In the following analysis, β_e is varied from 0% to 0.7% about the CYCLONE base case. The behavior of gyrokinetic simulations about CYCLONE for β_e values beyond what is presented here is the subject of ongoing study^{8,9} and not in the scope of what will be presented. For reference, the ideal magnetohydrodynamic (MHD) β -limit for this simulation is $\beta_e \sim 1.5\%$ under the artificial assumption $\alpha_{\text{MHD}} = 0$, as detailed in Ref. 5.

Figure 1 demonstrates the relative magnitude of ion and electron heat flux over the range of the β_e scan run with GYRO. The electron transport is divided into electrostatic and electromagnetic components, where the electrostatic component results from the radial component of $E \times B$ drifts and the electromagnetic component represents the radial motion of electrons caused by streaming along the total magnetic field (equilibrium plus perturbations). The ion diffusiv-

ity is almost entirely electrostatic because the dominant instability with CYCLONE parameters is the ion temperature gradient (ITG) instability. A physical explanation for the drop in ion transport with increasing β_e can be understood as β_e stabilizing the ITG instability by diverting energy into bending the fieldline.¹⁰ Over the range of β_e studied, the magnetic flutter component of electron transport increases from effectively zero to a fifth of the total transport or about 30% of the electron transport. The CYCLONE base case parameters are $R_0/a = 2.775$, $r/a = 0.5$, $T_e = T_i$, $R_0/L_{Te} = R_0/L_{Ti} = 6.99$, $R_0/L_n = 2.2$, $q = 1.4$, $s = 0.786$, and $v_{ei} = 0$. R_0 and a are the major and minor radii of the tokamak, T_e and T_i are the equilibrium electron and ion temperature, the temperature and density gradient length scales are defined as $L_{Te} = (d \ln T_e / dr)^{-1}$ and $L_{Ne} = (d \ln N_e / dr)^{-1}$, q is the magnetic safety factor with the magnetic shear $s = (r/q) \partial q / \partial r$, and v_{ei} is the electron–ion collision frequency normalized to c_s/a , where the sound speed $c_s = \sqrt{T_e / m_i}$. The CYCLONE geometry is a circular s - α geometry, with $\alpha = q^2 R d\beta / dr$ set to zero. In addition to varying β_e , we also use kinetic electrons with mass ratio $\mu = \sqrt{m_i / m_e} = 42$. This choice of mass ratio corresponds to a hydrogen plasma as opposed to deuterium and matches the value chosen in Refs. 3 and 5.

GYRO employs a fieldline following coordinate system using spatial variables (ψ, θ, α) , and the Clebsch representation¹¹ for the magnetic field $B_0 = \nabla \alpha \times \nabla \psi$. The coordinate ψ , equal to the poloidal flux divided by 2π in general geometries, is related to the midplane minor radius r for circular geometries. The fieldline label α relates to toroidal angle ϕ by $\alpha = \phi + v(r, \theta)$. Because r and α label fieldlines in the Clebsch representation, θ is both the poloidal angle and the position along a fieldline labeled by remaining coordinates (r, α) . The velocity grid of the presented data consists of 128 points (8 energies, 8 pitch angles, and 2 signs of velocity). The spatial grid consists of 14 parallel gridpoints for each sign of velocity, 120 radial gridpoints, and $k_{\perp} \rho_s$ values are (0, 0.084, 0.168, ..., 1.26) for a total of 16 toroidal modes. We use k_{\perp} to represent the component of the wavenumber in

^{a)}Paper N12 3, Bull. Am. Phys. Soc. 55, 193 (2010).^{b)}Invited speaker.

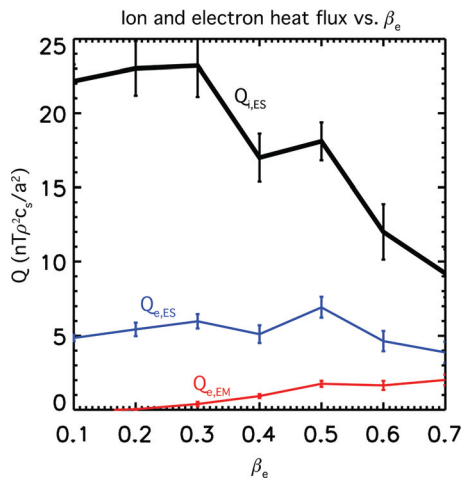


FIG. 1. (Color online) Ion (black), electron electrostatic (blue), and electron electromagnetic (red) heat flux vs β_e . Time averages are taken between $t = 150 c_s/a$ and $t = 500 c_s/a$

the direction perpendicular to both $\nabla\psi$ and magnetic field unit vector $\mathbf{b} = \mathbf{B}/B$. The sound radius $\rho_s = (m_i T_e)^{1/2}/eB$ with e being the magnitude of the charge on an electron.

Recent work on this β_e scan of the CYCLONE base case demonstrates widespread breaking of the magnetic fieldlines even at the lowest nonzero value of β_e .¹² The authors find that the broken surfaces do not result in a dramatic rise and transport and use the magnetic diffusion coefficient¹³ to describe observed levels of electron transport. Here, we expand on the results of Ref. 12 in several ways. We emphasize that the reconnection must be driven, nonlinearly that the stochastic structure is a consequence of interaction of islands of different order and extend the analysis beyond the CYCLONE base case to a simulation where the microtearing mode is the dominant instability. The paper is organized as follows. In Sec. II, we give a criterion (the resonance condition) for magnetic reconnection and demonstrate that it is satisfied for the lowest value of β_e in the CYCLONE scan. Upon observing reconnection, we produce Poincaré surface of section plots to analyze the structure of the field and demonstrate both that the field is stochastic and the stochasticity must be caused by interaction of islands of differing order. In Sec. III, we demonstrate a quantitative relation between the Rechester and Rosenbluth magnetic diffusion coefficient¹³ and electron heat transport. The predictions of electron heat flux are compared to output from GYRO, and this model is then applied to a simulation where the microtearing mode is the dominant instability.

II. RECONNECTION AND STOCHASTICITY

In GYRO, the magnetic potential A_{\parallel} is decomposed into Fourier harmonics given by

$$A_{\parallel}(r, \theta, \phi) = \sum_{j=N+1}^{j=N-1} A_{\parallel n}(r, \theta) \exp^{-in\alpha}, \quad (1)$$

with $n = j\Delta n$. To ensure A_{\parallel} is real, only $n_n = N + 1$ complex modes $j = 0, \dots, N$ are kept in the simulation with the requirement $A_{\parallel n}^* = A_{\parallel -n}$ for the negative j counterparts. A_{\parallel} then

causes magnetic reconnection if it satisfies the resonance condition,¹⁴ $m = n q(r)$. Here, n is the toroidal mode number and m is the poloidal mode number. In effect, this condition determines the radial locations where the magnetic potential $A_{\parallel}(n)$ is resonant. Because gyrokinetic simulations have discrete toroidal mode numbers, the resonance condition is satisfied at discrete radial locations determined by the safety factor

$$q(r) = m/n \approx q_0[1 - s(r - r_0)/r_0]. \quad (2)$$

The center of the simulation $r_0 = 0.5a$ is where the safety factor $q_0 = 1.4$. The minimum n value in the simulation is 12, with all other values of n being integer multiples of the minimum value. Because the smallest n value is quite large, we note that any reconnection observed must be caused by higher order islands—the lowest order resonant rational surfaces in the simulation domain are 14/12, 15/12, 16/12, and 17/12. The radial locations corresponding to these values are found using Eq. (2) with $n = 12$.

Once the radial locations of resonances have been determined, the proper toroidal mode number m must be singled out. This amounts to requiring A_{\parallel} to have a nonzero average parallel to the field at the rational surface locations $r = r_{\text{rat}}(n)$. In GYRO, it is equivalent to find the resonant component of A_{\parallel} by considering the parity of the magnetic potential with θ . Modes even in θ can be resonant while odd modes cannot. For the CYCLONE base case, the unstable ITG mode has even parity in ϕ , coupling to odd (ballooning) parity in A_{\parallel} . Because the fieldline average of the odd parity A_{\parallel} must vanish, any reconnection observed in our CYCLONE base-case simulations must be nonlinearly driven. An analysis of the parallel mode structure of eigenmodes in CYCLONE (ITG as well as damped modes) in relation to tearing parity is presented in Ref. 15.

As described in Ref. 12, nonlinear simulations do in fact cause reconnection. The resonant (even parity in θ) component of the magnetic potential can be obtained by taking the θ average δA_{\parallel} . The q profile in CYCLONE combined with the toroidal mode number resolution will determine the radial positions of rational surfaces.

$$A_{\parallel}^{\text{res}} = \langle A_{\parallel}(r = r_{\text{rat}}, n, \theta) \rangle_{\theta}. \quad (3)$$

Figure 2 displays the resonant component of A_{\parallel} ($n = 12$) versus radius and time for $\beta_e = 0.1\%$ on a log scale. The lines located at $r = 2.97\rho_s$, $17.86\rho_s$, $32.74\rho_s$, and $47.62\rho_s$ are the rational surface locations of the fundamental mode ($n = 12$ or $k_{\perp}\rho_s = 0.087$) in the simulation. Because the allowed toroidal mode numbers in GYRO are integer multiples of the fundamental, the four radial locations listed are rational surfaces for all modes in the simulation. The fact that the intensity does not vanish on rational surface locations ensures that reconnection has occurred, even at the lowest value of β_e simulated. What we cannot tell from Fig. 2 is what type of reconnection occurs. Depending on the strength of the perturbation, islands created by reconnection may be large enough to overlap with neighboring islands causing stochasticity¹⁶ or be small enough to be isolated from each other. Should the answer be widespread stochasticity,

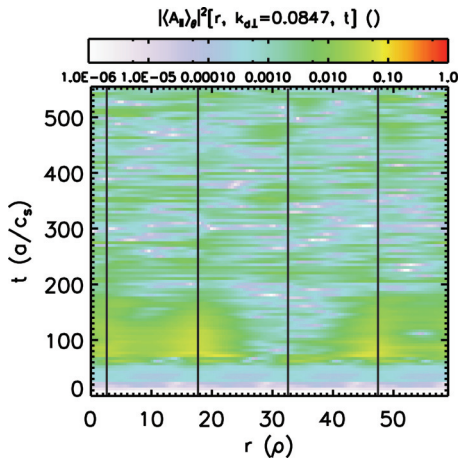


FIG. 2. (Color online) Resonant intensity of magnetic potential vs radius and time. Vertical lines are rational surface locations. Finite amplitude at rational surface locations indicates reconnection has occurred.

electrons would be free to travel across magnetic surfaces by parallel streaming and would raise significant concerns for the electron heat conductivity.

One tool to analyze how the reconnection is manifested is Poincaré surface of section plots. A surface of section plot is created by tracking the trajectory of a magnetic fieldline (r_0, α_0) and recording updated values (r_i, α_i) each time the fieldline crosses the outboard midplane. With the Clebsch representation, unperturbed fieldline trajectories are very straightforward to lowest order in gyrokinetic expansion

$$\frac{d\psi}{d\ell} = \frac{1}{B} \mathbf{B} \cdot \nabla \psi \approx \frac{1}{B} \mathbf{B}_0 \cdot \nabla \psi = 0, \quad (4)$$

$$\frac{d\alpha}{d\ell} = \frac{1}{B} \mathbf{B} \cdot \nabla \alpha \approx \frac{1}{B} \mathbf{B}_0 \cdot \nabla \alpha = 0, \quad (5)$$

$$\frac{d\theta}{d\ell} = \frac{1}{B} \mathbf{B} \cdot \nabla \theta = \frac{1}{J_{\psi} B}, \quad (6)$$

where the Jacobian J_{ψ} is defined as

$$J_{\psi} = \frac{1}{(\nabla \alpha \times \nabla \psi) \cdot \nabla \theta}. \quad (7)$$

These equations serve to define ℓ , the distance travelled along a fieldline. For the circular flux-surface magnetic geometry employed in our simulations $\Delta \ell = 2\pi qR$ for one full poloidal circuit $\Delta \theta = 2\pi$. Equations (4)–(6) demonstrate that without magnetic perturbations, the fieldline labels ψ and α do not evolve. The equilibrium fieldlines are periodic in coordinates (ϕ, θ) , but θ is NOT periodic in coordinates (α, θ) , where GYRO simulations typically cover a partial torus with toroidal domain $0 \leq \phi \leq 2\pi/\Delta n$. To account for the change in α over a full integration in θ , the fieldline labels α_+ at $\theta = \pi$ and α_- at $\theta = -\pi$ are related by,

$$\alpha_- = \alpha_+ + 2\pi q, \quad (8)$$

consistent with the partial torus domain. Accordingly, integrating from $\theta = \pi$ to $\theta = -\pi$ causes $\alpha \rightarrow \alpha + 2\pi q$. This representation of α is periodic over the partial toroidal domain, providing a rule for mapping alpha back into the interval $-\pi\Delta n < \alpha < \pi\Delta n$.

The perturbed magnetic field $\delta \mathbf{B}$ is given by $\delta \mathbf{B} = \nabla \times (A_{\parallel} \mathbf{b}) \approx (\nabla A_{\parallel}) \times \mathbf{b}$. Inserting this into Eqs. (4) and (5) we find, at first order in ρ/R , that the perturbed field-line trajectories are given by

$$\frac{\partial \alpha}{\partial \ell} = \frac{\partial A_{\parallel}}{\partial \psi}, \quad \frac{\partial \psi}{\partial \ell} = -\frac{\partial A_{\parallel}}{\partial \alpha}. \quad (9)$$

The prescription for producing a Poincaré plot consists of integrating Eq. (9) over $-\pi qR \leq \ell \leq \pi qR$ from initial coordinates (r_0, α_0) to obtain new coordinates (r_1, α_1) . The new value of α_1 is then modified by $2\pi q(r)$ to account for Eq. (8). Final coordinates (r_1, α_1) are recorded and given a dot on a plot with x axis r and y axis α , and the integration procedure is repeated to produce (r_2, α_2) , and hence a new dot. All Poincaré plots in the present paper were created using 100 initial conditions with each initial condition followed 3000 revolutions in θ . The initial conditions run diagonally through the map, starting with $r = 0, \alpha = -\pi$ up to roughly $r = 58, \alpha = \pi$.

Figure 3 demonstrates that the magnetic surfaces are destroyed for even the lowest value of β_e . Islands of stability are larger and more prevalent for the $\beta_e = 0.1\%$ compared with $\beta_e = 0.7\%$. The chaotic fieldlines are surprising to see because the magnetic component of electron heat flux is very near zero in the low β_e case. It is instructive to compare the width of magnetic islands to the separation between

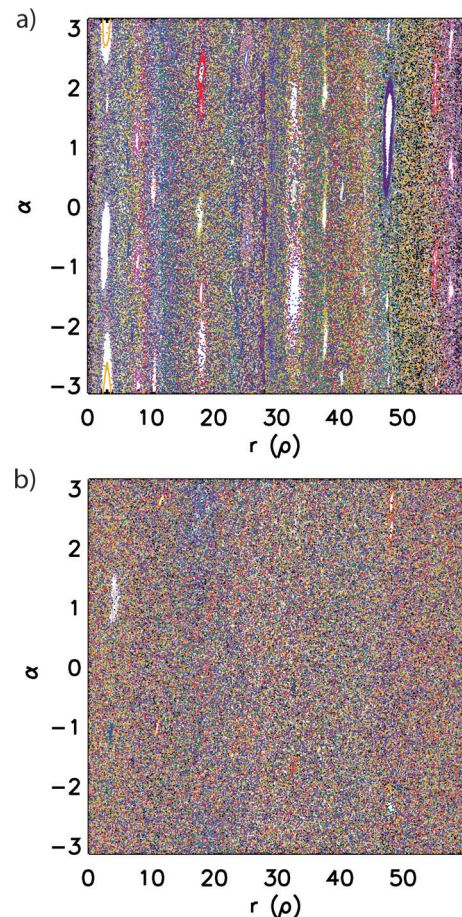


FIG. 3. (Color online) Poincaré map for $t = 450 a/c_s$ demonstrating stochastic sea at (a) $\beta_e = 0.1\%$ and (b) $\beta_e = 0.7\%$.

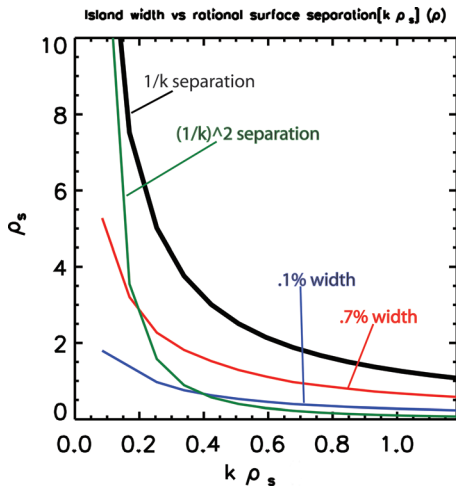


FIG. 4. (Color online) Rational surface separation for constant $k_{\perp}\rho_s$ (black) and neighboring modes (green) vs island width of $\beta_e = 0.7\%$ (red) and $\beta_e = 0.1\%$ (blue).

rational surface locations to understand why the surfaces are destroyed,

$$w_{\text{island}} = 4\sqrt{\frac{qR}{sB}}|A_{\parallel}|, \quad (10)$$

$$w_{\text{separation}} = \frac{1}{k_{\perp}s}. \quad (11)$$

Equation (11) defines the radial separation between resonant rational surfaces corresponding to a fixed $k_{\perp}\rho_s$. If the width of an island created is larger than the distance to the next island, the field structure will be chaotic (Ref. 16). Using

Eqs. (10) and (11), we see the intensity of $A_{\parallel}(k_{\theta})$ is not large enough to create an island of a given $k_{\perp}\rho$, whose width is larger than the separation between resonant surfaces $1/k_{\perp}s$ for all values of β_e and $k_{\perp}\rho_s$ (Fig. 4). However, this interpretation ignores the fact that island overlap can occur between resonances of different order. Because all toroidal modes are integer multiples of the fundamental $n_0 = 12$, the minimum radial separation w_{min} between a resonance arising from n and $n + 12$ is much smaller than the separation of resonances for a fixed n ,

$$w_{\text{min}} \approx \frac{\Delta k_{\perp}}{k_{\perp}^2 s}, \quad (12)$$

where $\Delta k_{\perp}\rho_s = 0.084$ is the increment between neighboring values of $k_{\perp}\rho$. The $1/k^2$ line in Fig. 4 is Eq. (12), and it indicates that island overlap occurs between adjacent modes at higher perpendicular modes. Figure 5 explores this phenomenon. The leftmost column is the surface of section plot using Eq. (9) using only $A(k_{\perp}\rho = 0.084)$ or the lowest allowed value of n in Eq. (1) for the integration. The second column is created by keeping the first two modes of the system, $A(k_{\perp}\rho = 0.084) + A(k_{\perp}\rho = 0.168)$, while the third and fourth columns also include $A(k_{\perp}\rho = 0.252)$ and $A(k_{\perp}\rho = 0.252) + A(k_{\perp}\rho = 0.336)$, respectively. The crossing of Eq. (12) with the $\beta_e = 0.1\%$ in Fig. 4 indicates island overlap to occur for roughly $k_{\perp}\rho > 0.4$, and we see the last column of Fig. 5(a) does not produce widespread stochasticity. The intersection between Eq. (12) and island width of $\beta_e = 0.7\%$ occurs for $k_{\perp}\rho > 0.2$, and we indeed see chaotic trajectories beginning with the second column of Fig. 5 and fully developed in the third column. We conclude that the widespread stochasticity found in gyrokinetic simulations of

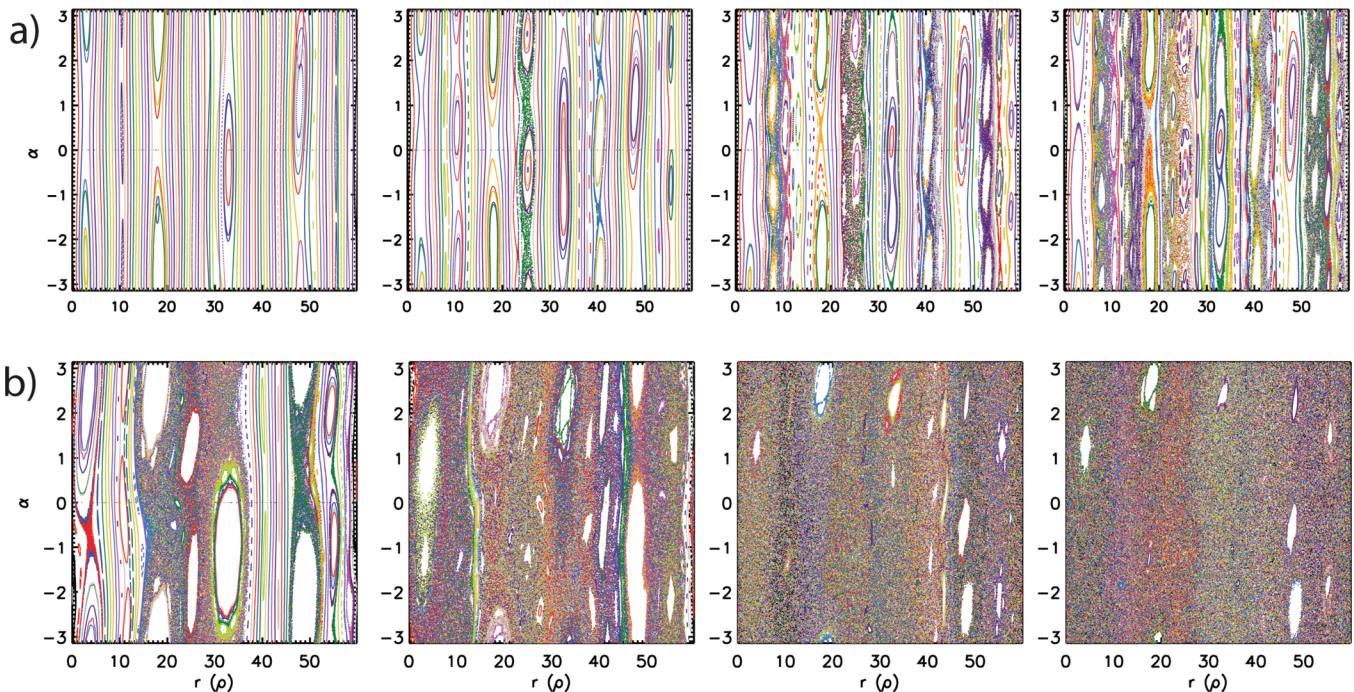


FIG. 5. (Color online) Poincaré plots for $t = 450 c_s/a$ and (a) $\beta_e = 0.1\%$ and (b) $\beta_e = 0.7\%$, where an increasing number of toroidal modes are kept. The first column corresponds to the field trajectories of only $k_{\perp}\rho_s = 0.084$, second including $k_{\perp}\rho_s = 0.084$ and 0.168 , third including $k_{\perp}\rho_s = 0.084, 0.168$, and 0.252 , and the last column $k_{\perp}\rho_s = 0.084, 0.168, 0.252$, and 0.336 .

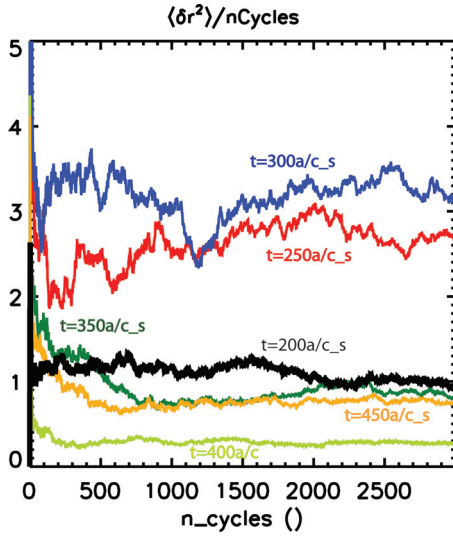


FIG. 6. (Color online) $d_m * (2 * 2\pi qR)$ as a function of turns around the tokamak for $\beta_e = 0.7\%$.

CYCLONE parameters is necessarily a consequence of interaction of islands of differing order.

III. QUANTIFYING TRANSPORT CAUSED BY STOCHASTIC FIELDS

The lack of electron heat transport despite evidence of widespread destruction of magnetic surfaces requires a nuanced interpretation of transport in chaotic fieldline trajectories. An intuitive way to start would be by considering the mean-squared radial displacement versus poloidal crossings. The magnetic diffusion coefficient,¹³ defined in Eq. (13), is a means of quantifying the degree of stochasticity in the fields. Poincaré surface of section plots created in Sec. II provides a direct method of calculating the magnetic diffusion coefficient, d_m , given by

$$d_m = \lim_{\ell \rightarrow \infty} \frac{\langle [r_i(\ell) - r_i(0)]^2 \rangle}{2\ell} \approx \lim_{\ell \rightarrow \infty} \frac{1}{2\ell N} \sum_{i=1}^N [r_i(\ell) - r_i(0)]^2. \quad (13)$$

Note that d_m has units of length. In the last step of Eq. (13), we have averaged over the 100 individual fieldlines followed in the plots. Figure 6 gives the magnetic diffusion coefficient for several independent time slices for $\beta_e = 0.7\%$. d_m is well estimated by taking the average value between 1500 and 3000 turns because the values trend to a constant, with variations over cycle number n_{cycle} , within a single time slice being significantly less than the variation between time slices. By producing surface of section plots at each time slice of simulation, the time dependence of d_m can be calculated and compared to the time dependence of the electron heat flux observed in our simulations.

Reference 17 describes an exact relation between the magnetic diffusion coefficient d_m and associated electron heat flux Q_{st} in the collisionless limit, appropriate for the CYCLONE base case. However, we caution the reader in that Ref. 17 assumes a relation between the ambipolar

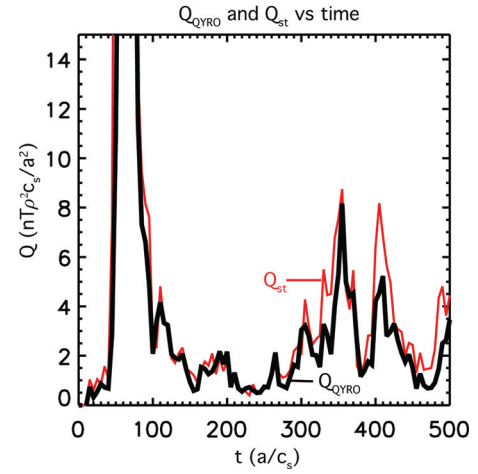


FIG. 7. (Color online) Stochastic heat transport Q_{GYRO} (black) and Q_{st} (red) vs time at $\beta_e = 0.7\%$.

electric field, created from electrons diffusing by radial streaming relative to static ions, to the density and temperature gradients of the equilibrium to derive the equation below. It is far from clear that this assumption will be valid in a flux tube simulation, where there is no average radial electric field, and a more rigorous connection between d_m and Q_{st} is the subject of ongoing investigation. Nevertheless, we present this model of stochastic heat transport found between Eqs. (6) and (7) in Ref. 17 as a “working model” for the energy flux,

$$Q_{st} = -2\sqrt{\frac{2}{\pi}} d_m v_{th} \left(\frac{\partial T}{\partial r} \right) (f_p n). \quad (14)$$

Above, $v_{th} = \sqrt{T/m}$ is the thermal velocity of the particle. To compare this to the transport output by GYRO, the density in Eq. (14) is modified from the original reference in that it must be multiplied by the passing particle fraction ($f_p \approx 1 - \sqrt{r/R} \approx 55\%$ in CYCLONE) because trapped particles are confined about the outboard midplane and will not follow the stochastic fieldlines over long distances. The resulting stochastic electron heat flux is then obtained by combining Eqs. (13) and (14). Figure 7 shows the excellent agreement between the stochastic transport model and the actual output from GYRO in both magnitude and time behavior. Figure 8 shows this agreement over the range of the β_e scan.

A. Stochastic transport for microtearing unstable simulation

We conclude our analysis by applying the working model of stochastic transport to a nonlinear simulation, where the magnetic component of electron transport consists of greater than 97% of the total transport in the simulation. The local simulation aims to model the National Spherical Torus Experiment (NSTX) discharge 120968, which is included in a set of confinement scaling experiments.^{18,19} The numerically reconstructed equilibrium is used as well as the measured physical parameters at $r/a = 0.6$, $T_i/T_e = 0.95$, $a/L_{Ni,Ne} = -0.83$, $a/L_{Ti} = 2.4$, $a/L_{Te} = 3.7$, $\mu = 60$, $s = 1.7$,

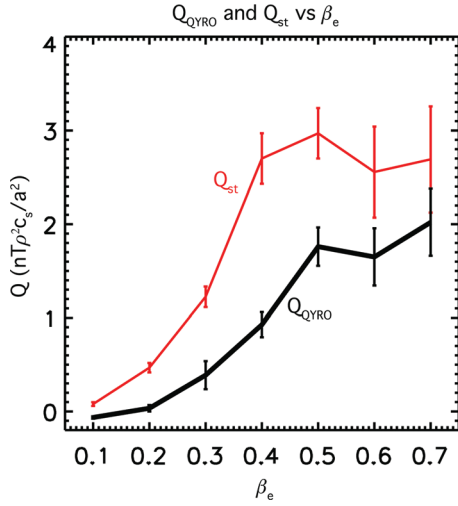


FIG. 8. (Color online) Stochastic heat transport Q_{GYRO} (black) and Q_{st} (red). Time averages were taken between $t = 150 c_s/a$ and $t = 500 c_s/a$ vs β_e .

$\rho_* = 0.0075$, $q = 1.7$, and $v_{ei} = 1.46$. The spatial resolution includes 8 toroidal modes ($k_{\perp} = 0, 0.105, \dots, 0.735$) and 400 radial gridpoints, while velocity space contains 192 points (8 energies, 12 pitch angles and 2 signs of velocity). At this radial location the only linear instability present is the microtearing mode, which has been observed previously in some spherical tokamak discharges.^{20–22}

This simulation contains a finite value of collisionality (required for the microtearing mode to be unstable), bringing into question whether Eq. (14), which is produced in the collisionless limit, is the appropriate relation between d_m and Q_{st} . The electron mean free path is roughly 12.5 m, while the stochastic correlation length^{13,16} $L_c = \pi R / \ln(0.5\pi * \hat{s}) \approx 2.5$ m. Because the mean free path is significantly longer than the correlation length, the collisionless limit relating d_m and Q_{st} is still appropriate. As with CYCLONE, widespread stochasticity is observed (Fig. 9). Unlike the CYCLONE base case, the amplitude of A_{\parallel} in the microtearing case is large the amplitude of A_{\parallel} is large enough so that the island width of $A_{\parallel}(n)$ is larger than the rational surface separation

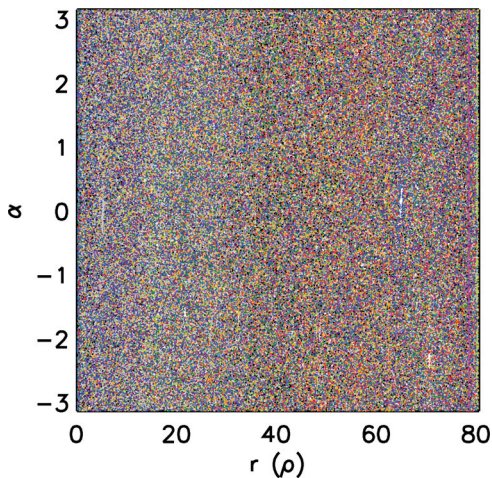


FIG. 9. (Color online) Representative Poincaré plot for simulation of NSTX shot 120968.

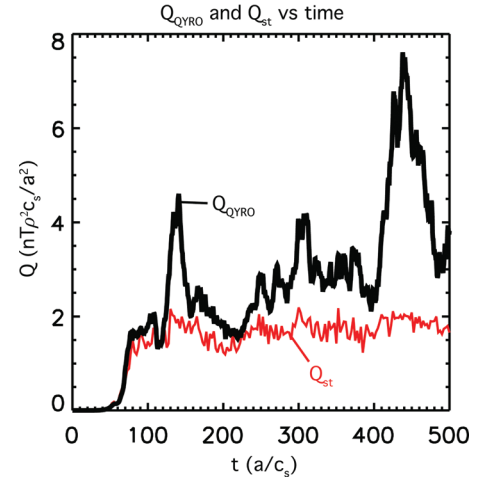


FIG. 10. (Color online) Q_{GYRO} (black) and Q_{st} (red) vs time in NSTX shot 120968.

$1/k_{\perp} s$ for all but the lowest two toroidal modes. Figure 10 plots Q_{st} and the output heat flux from GYRO versus time. The stochastic heat transport model does an excellent job of predicting the baseline level of transport, but fails to describe bursts in transport, whose magnitude can be triple that of the baseline. The bursts in transport are caused individually by the lowest $k_{\perp} \rho$ modes in the system. To understand why the stochastic heat transport model fails to agree with the bursts in transport in Fig. 10, we begin by noting

$$Q_{em} = \left\langle \int d^3v \frac{1}{2} m v^2 v_{\parallel} \frac{\delta B_r}{B_0} \delta f \right\rangle, \quad (15)$$

where $\langle A \rangle$ is the flux surface average of a quantity. In general, the drift kinetic equation would solve for the electron perturbed distribution function δf ,

$$\frac{\partial \delta f}{\partial t} + v_{\parallel} \frac{\partial \delta f}{\partial \ell} + \left[v_{\parallel} \frac{\delta B_r}{B} + \frac{(\delta E \times B)_r}{B_0^2} \right] \frac{\partial f_0}{\partial r} + q v_{\parallel} E_{\parallel} \frac{\partial f_0}{\partial v_{\parallel}} = 0. \quad (16)$$

The stochastic transport model assumes parallel streaming is the dominant effect on perturbed electrons and consequently only keeps the second and third terms in Eq. (16). Missing from the Rechester Rosenbluth treatment, but nonetheless potentially still of the same order are terms containing the perturbed electric field, high frequency perturbations, and the response to the parallel electric field. Keeping only the second and third terms of Eq. (16), we find the following solution for δf :

$$\delta f_{v_{\parallel} > 0}(\ell) = - \int_{-\infty}^{\ell} d\ell' \left[\frac{\delta B_r(\ell')}{B_0} \right] \frac{\partial f_0}{\partial r}, \quad (17)$$

$$\delta f_{v_{\parallel} < 0}(\ell) = + \int_{\ell}^{\infty} d\ell' \left[\frac{\delta B_r(\ell')}{B_0} \right] \frac{\partial f_0}{\partial r}. \quad (18)$$

Equations (17) and (18) are then used in Eq. (15) to obtain the stochastic heat flux,

$$Q_{st} \approx d_m \int d^3v \frac{1}{2} m v^2 |v_{\parallel}| \frac{\partial F_0}{\partial r}, \quad (19)$$

where we used the fact that

$$d_m = \frac{1}{2\pi q R} \int_{-\pi q R}^{\pi q R} d\ell \int_{-\infty}^{\infty} d\ell' \frac{dB_r(\ell) dB_r(\ell')}{B_0^2}. \quad (20)$$

The definition of Eq. (20) is equivalent to that given in Eq. (13) above (see, for example, Ref. 17). The fact that the Rechester Rosenbluth model does so well in Fig. 7 suggests that parallel streaming is the only important effect in electromagnetic electron heat transport for the CYCLONE base case, while the disagreement between Q_{st} and Q_{GYRO} indicates correlations between the vector potential and perturbed electric field contribute to the bursts in electron electromagnetic transport. High frequency perturbations (where the $\partial f/\partial t$ term might be important) were not observed in these simulations.

Outside of stochastic transport, there are many interesting and important results arising from nonlinear simulations of the microtearing mode. A complete analysis of this simulation, including a parameter scan and interpretation of the results, is left for a separate publication.²³

IV. CONCLUSIONS

In the present paper, we have demonstrated magnetic reconnection and stochasticity occurring in gyrokinetic simulations of the CYCLONE base case when electromagnetic effects and kinetic electrons are included. The destruction of magnetic surfaces must be nonlinearly driven and is caused by interaction between islands of different order. The stochasticity does not necessarily correspond to an increase in electron heat flux and is quantified by the magnetic diffusion coefficient. Although assumptions in the derivation are suspect for flux tube simulations, Ref. 17 provides a working model to estimate the stochastic heat flux from d_m in the collisionless limit. By using the fraction of passing particles in Eq. (14), the predicted stochastic heat flux is in excellent agreement with the output from GYRO in both time behavior and magnitude over the β_e scan. This estimate of stochastic energy transport is then applied to an experimentally relevant operating point where almost all of the transport is accounted by the magnetic component of electron transport. In this case, the stochastic transport model accurately predicts the baseline level of transport but fails to describe intermittent bursts caused by the lowest modes in the system. In conclusion, the presented findings suggest that eradication of magnetic surfaces on the microscale could be a ubiquitous phenomenon. The electron heat transport associated with chaotic surfaces is well described by the magnetic diffusion coefficient d_m . A rigorous relation between d_m and Q_{st} and

full analysis of the microtearing simulation are the subjects of ongoing research.

ACKNOWLEDGMENTS

The authors gratefully acknowledge the National Center for Computational Sciences at ORNL for providing computer resources under INCITE award FUS023. We also thank important conversations of M. J. Puschel, who has also demonstrated that plasma microturbulence produces magnetic stochasticity over this beta scan using the GENE code. This work was performed under the auspices of the U.S. Department of Energy by Lawrence Livermore National Laboratory under Contract DE-AC52-07NA27344, by General Atomics under Contract Number DE-FG03-95ER54309, and by Princeton Plasma Physics Laboratory Contract Number DE-AC02-09CH11466.

¹J. Candy and R. E. Waltz, *J. Comput. Phys.* **186**, 545 (2003).

²W. Dorland, F. Jenko, M. Kotschenreuther, and B. N. Rogers, *Phys. Rev. Lett.* **85**, 5579 (2000).

³Y. Chen and S. Parker, *J. Comput. Phys.* **189**, 463 (2003).

⁴A. G. Peeters, Y. Camenen, F. J. Casson, W. A. Hornsby, A. P. Snodin, D. Strintzi, and G. Szepesi, *Comput. Phys. Commun.* **180**, 2650 (2009).

⁵J. Candy, *Phys. Plasmas* **12**, 072307 (2005).

⁶M. J. Puschel, M. Kammerer, and F. Jenko, *Phys. Plasmas* **15**, 102310 (2008).

⁷A. M. Dimits, G. Bateman, M. A. Beer, B. I. Cohen, W. Dorland, G. W. Hammett, C. Kim, J. E. Kinsey, M. Kotschenreuther, A. H. Kritiz, L. L. Lao, J. Mandrekas, W. M. Nevins, S. E. Parker, A. J. Redd, D. E. Schumaker, R. Sydora, and J. Weiland, *Phys. Plasmas* **7**, 969 (2000).

⁸R. E. Waltz, *Phys. Plasmas* **17**, 072501 (2010).

⁹M. J. Puschel and F. Jenko, *Phys. Plasmas* **17**, 062307 (2010).

¹⁰J. Y. Kim, W. Horton, and J. Q. Dong, *Phys. Fluids B* **5**(11), 4030 (1993).

¹¹M. D. Kruskal and R. M. Kulsrud, *Phys. Fluids*, **1**, 265 (1958).

¹²W. M. Nevins, E. Wang, and J. Candy, *Phys. Rev. Lett.* **106**, 065003 (2011).

¹³A. B. Rechester and M. N. Rosenbluth, *Phys. Rev. Lett.* **40**, 38 (1978).

¹⁴A. H. Reiman and D. A. Monticello, *Nucl. Fusion* **32**, 1341 (1992).

¹⁵D. R. Hatch, P. W. Terry, F. Jenko, F. Merz, M. J. Puschel, W. M. Nevins, and E. Wang, "Role of subdominant modes in plasma microturbulence," *Phys. Plasmas* **55**, (2010); Paper XII 2, Bull. Am. Phys. Soc. **55**, 371 (2010).

¹⁶G. M. Zaslavsky and B. V. Chirikov, *Sov. Phys. Usp.* **14**, 549 (1972).

¹⁷R. W. Harvey, M. G. McCoy, J. Y. Hsu, and A. A. Mirin, *Phys. Rev. Lett.* **47**, 102105 (1981).

¹⁸S. M. Kaye, R. E. Bell, D. Gates, B. P. LeBlanc, F. M. Levinton, J. E. Menard, D. Mueller, G. Rewoldt, S. A. Sabbagh, W. Wang, and H. Yuh, *Phys. Rev. Lett.* **98**, 175002 (2007).

¹⁹S. M. Kaye, F. M. Levinton, D. Stutman, K. Tritz, H. Yuh, M. G. Bell, R. E. Bell, C. W. Domier, D. Gates, W. Horton, J. Kim, B. P. LeBlanc, N. C. Luhmann, Jr., R. Maingi, E. Mazzucato, J. E. Menard, D. Mikkelsen, D. Mueller, H. Park, G. Rewoldt, S. A. Sabbagh, D. R. Smith, and W. Wang, *Nucl. Fusion* **47**, 499 (2007).

²⁰D. J. Applegate, C. M. Roach, J. W. Connor, S. C. Cowley, W. Dorland, R. J. Hastie, and N. Joiner, *Plasma Phys. Controlled Fusion* **49**, 1113 (2007).

²¹K. L. Wong, S. Kaye, D. R. Mikkelsen, J. A. Krommes, K. Hill, R. Bell, and B. LeBlanc, *Phys. Rev. Lett.* **99**, 135003 (2007).

²²K. L. Wong, S. Kaye, D. R. Mikkelsen, J. A. Krommes, K. Hill, R. Bell, and B. LeBlanc, *Phys. Plasmas* **15**, 056108 (2008).

²³W. Guttenfelder et al., *Phys. Rev. Lett.* **106**, 155004 (2011).